## Automated Characterization of Macroscale Tissue 3D Spatial Material Properties via Robotically-Directed Impedimetric Sensing

Ezgi Kucukdeger<sup>®</sup>, Yujing Zhang, Junru Zhang, Yang Liu, Xiaoting Jia<sup>®</sup>, Member, IEEE, and Blake N. Johnson<sup>®</sup>

Abstract-Here, we report a novel method for automated characterization of bulk tissue 3D spatial properties based on reverse engineering-driven non-planar tool path planning and robotically-directed sensing. The method incorporates information on object (e.g., tissue) and inspection tool (e.g., sensor) geometry for automated inspection of tissue mechanical and dielectric properties across macroscopic nonplanar domains as large as 44 cm<sup>2</sup>. The process avoids the need for manual sensortissue integration processes. The impact and the utility of the method were demonstrated by automated mapping of 3D spatial distributions of mechanical and dielectric properties of plant and animal tissues using multiple complementary impedimetricbased sensors of varying types and form factor, including rigid micro-electromechanical systems (MEMS) and flexible multifunctional fibers. Applications to automated characterization of food quality (e.g., type and age) are provided, including 3D spatial mapping of plant and animal tissue mechanical and dielectric property distributions. Ultimately, automated methods for 3D spatial inspection of plant and animal tissue properties are critical to agriculture, food processing, organ transplantation, and biomanufacturing industries.

Note to Practitioners—This article is motivated by the need for automating the inspection of soft 3D biological objects. Here, we present a method that generates 3D quality maps of tissue properties using several sensors. The proposed tool path planning program outputs a customized tissue-conforming path for inspection based on the topographical features of the tissue. Hence, this method enables high-throughput, spatially-resolved, minimally-invasive, and reliable inspection of soft 3D biological objects. Applications to inspection of food quality were provided using two impedimetric-based sensors. Practitioners can directly

Manuscript received 16 December 2022; revised 5 April 2023; accepted 19 May 2023. This article was recommended for publication by Associate Editor Q. Xu and Editor L. Zhang upon evaluation of the reviewers' comments. This work was supported in part by GlycoMIP, a National Science Foundation Materials Innovation Platform funded through Cooperative Agreement under Grant DMR-1933525. The work of Blake N. Johnson was supported by the National Science Foundation under Grant CBET-1650601 and Grant CMMI-1739318. (Corresponding author: Blake N. Johnson.)

Ezgi Kucukdeger, Junru Zhang, and Yang Liu are with the Grado Department of Industrial and Systems Engineering, Virginia Tech, Blacksburg, VA 24061 USA.

Yujing Zhang and Xiaoting Jia are with the Bradley Department of Electrical and Computer Engineering, Virginia Tech, Blacksburg, VA 24061 USA.

Blake N. Johnson is with the Grado Department of Industrial and Systems Engineering, Department of Materials Science and Engineering, and the Department of Chemical Engineering, Virginia Tech, Blacksburg, VA 24061 USA (e-mail: bnj@vt.edu).

This article has supplementary material provided by the authors and color versions of one or more figures available at https://doi.org/10.1109/TASE.2023.3279338.

Digital Object Identifier 10.1109/TASE.2023.3279338

apply the framework to inspection of other tissue properties and soft objects. This work provides an advance in automated methods for inspection, and real-time monitoring of tissue 3D property distributions, which reduces the need for manual tissue handling and requirement for sensor-product interface prior to characterization. This work can be implemented in various biomanufacturing applications and industries, including food safety and quality control, tissue engineering, and organ transplantation, to ensure the quality and safety of macroscopic tissue-engineered medical and food products.

Index Terms—Automated sensing, bioimpedance imaging, nonplanar path planning, high-throughput characterization, automated inspection.

#### I. Introduction

UTOMATED inspection methods provide economical, convenient, and accurate quantitative analysis of samples and products in various industries including agriculture, pharmaceutical, and biotechnology [1], [2], [3]. Commonly, fluorescence microscopy is used as a noninvasive inspection tool in life-science studies as it enables the visual inspection of biological specimens with sizes ranging from sub-micrometers to millimeters [4]. However, recent developments in biotechnology have shifted the focus of inspection from molecular and cellular products to tissue-based systems and products, including mesoscopic (i.e., millimeter to centimeter) and macroscopic tissues and organs [5], [6], [7]. Impedimetric sensing methods have emerged as versatile measurement format for quantification and monitoring of various tissue characteristics, including composition [8], [9], [10], cell viability [11], cell type [12], extent of differentiation [13], [14], chemosensitivity [15], and organ assessment [16]. Thus, impedimetric sensing can be leveraged for monitoring various tissue characteristics, properties, and physiological processes.

Ensuring the quality and safety of macroscopic tissue-based products are essential in various areas including the food industry [17], tissue engineering [18], [19], and organ transplantation [20]. Sensing of tissue impedance via surface contact electrodes, often referred to as bioimpedance monitoring, has been leveraged for the assessment of health and quality of animal and plant tissues, such as engineered animal and plant tissues and foods, as it enables monitoring of tissue composition, structure, and physiological processes [17], [21], [22], [23], [24]. Electrical Impedance Spectroscopy

1545-5955 © 2023 IEEE. Personal use is permitted, but republication/redistribution requires IEEE permission. See https://www.ieee.org/publications/rights/index.html for more information.

(EIS) via surface-based two-, three- and four-electrode configurations has been used as a non-destructive inspection method to characterize various fruits and vegetables including apples, bananas, lettuce, mangoes, and strawberries [21], [22]. For example, Chowdhury et al. showed that the electrical impedance of bananas was correlated with the ripening process by analyzing impedance and phase angles in a frequency range from 50 Hz to 1 MHz for 6 days [23]. Yovcheva et al. argued that the changes in the electrical properties of the apples can be attributed to the changes in the relative moisture content during aging [24]. They performed impedance measurements in a frequency range from 30 Hz to 30 MHz on the cylindrical samples cut from the apples with a length of 46 mm and a diameter of 20 mm. Ibba et al. evaluated the impedance changes on apples and bananas for 13 days and showed the relationship between fruit ripening and the impedance in a frequency range from 100 Hz to 85 kHz [22]. They used a total of four electrodes placed at a 3 cm distance and then averaged the measurements obtained from multiple twoelectrode configurations to achieve an output representing the entire fruit. Also, Mousa et al. showed the effect of the freezing and heating injuries on the bioimpedance of several vegetables including tomatoes, eggplants, and cucumbers over a frequency range of 10 Hz to 200 kHz using 2 electrodesconfiguration [25]. Recently, Yoshimoto-Haramura et al. used bioimpedance measurements to predict the percentage of liver steatosis which is considered a main reason for graft failure after transplantation at multiple frequencies ranging from 2 to 100 kHz using a Fish analyzer DFA 100 which is based on the tetrapolar circuit method [26].

Although bioimpedance monitoring enables noninvasive and real-time characterization of bulk macroscale tissues and organs, the majority of measurement formats are performed at a single location and do not yield spatial information [27]. However, there remains a need to verify the spatial distribution of tissue bioimpedance [27], in addition to other tissue properties. Scanning electrochemical microscopy (SECM), microelectrode arrays (MEA), and electrical impedance tomography are among the spatial impedimetric sensing methods that have been developed and used in various studies [27]. However, these methods cannot be applied to generate 3D property maps for characterization of the samples with freeform surfaces, since their applications are limited to samples with flat surfaces, 2D impedance maps, and the use of fixed multiple-electrodes probes [27], [28]. To address this challenge, conforming thin film-based systems have been utilized for spatial mapping of bulk tissues and organs [29], yet require manual tissue handling processes associated with sensor-tissue integration. Hence, it is essential to develop flexible and automated methods capable of providing mapping of bulk tissue and organ 3D spatial properties that require minimal manual processes (e.g., associated with sensor-tissue integration) and requirement for sensor-tissue integration prior to characterization.

The reliability of automated tissue inspection methods depends on precise control of the sensing tool's position since the performance of electrical impedance measurements relies on the contact area between the sensing electrodes and the specimen [30]. Therefore, manual position control of the sensing tool limits the accuracy and reliability of the sensing system [30]. Recently, several researchers have investigated robot-assisted electrical impedimetric-based sensing systems [28], [30]. For example, Cheng et al. presented an electrical impedimetric-based system that generates crosssectional 2D impedance maps for detection of heterogeneous elements under the sample's surface by scanning the target area given by the user [28]. Penza et al. incorporated a stereo vision system to control the motion of the robotic system for electrical impedimetric-based scanning of a target tissue surface to discriminate the tumor location [30]. Even though path planning for electrical impedimetric-based scanning applications is an emerging area, computer-aided inspection planning for touch-based probes and coordinate measuring machines (CMM) has been widely studied for automated inspections of manufactured parts [31]. The main constraint in inspection path planning is collision detection and automatic avoidance of obstacles since the sensing tool or tool holder may collide with the sample and damage both the tool and sample [31], [32]. Various approaches have been proposed to generate collisionfree scanning paths for CMMs [31], [32], [33], [34], [35]. For example, Zhao et al. combined a laser scanner and a touch-trigger probe to create collision-free inspection plans for CMM using the product and manufacturing information data contained in the computer-aided design (CAD) model of the part [33]. Later, Mineo et al. proposed a Mesh Following Technique to generate tool paths directly from the points on the tessellated model (i.e., mesh) without curve fitting and approximation steps [34]. Recently, Liu et al. presented an optimal path planning system that minimizes the total inspection time for free-form auto body surfaces using simulated annealingbased optimization algorithm [32]. However, CAD or mesh models containing the topographic information of the part are required inputs for the inspection path planning applications. Reverse engineering (RE) techniques, such as 3D scanning, computed tomography, and magnetic resonance imaging, are utilized to obtain 3D models of organs or other anatomical structures in the absence of an existing CAD model [36], [37]. Thus, new methods for inspection path planning that synergize with 3D scanning-based reverse engineering workflows could enable the spatial impedimetric characterization of macroscale tissues and organs with freeform surfaces. In addition, there remains a need to characterize additional properties, such as mechanical properties [18].

Here, we report a novel method for automated characterization of bulk tissue and organ 3D spatial properties based on reverse engineering-driven non-planar tool path planning and robotically-directed sensing. Our adapted point cloud-based path planning (PCPP) algorithm generates a customized sensing path based on the tissue surface geometry acquired by the 3D scanning system, enabling spatially resolved high-throughput sensing across the inspection area specified by the user. We demonstrate automated 3D spatial mapping of bulk tissue impedance and mechanical properties using real-time impedimetric monitoring via multifunctional fiber and piezoelectric cantilever sensors, respectively. Applications to inspection of food quality were provided, including potential

for automated inspection of meat and fruit type, composition, and age. This work provides an advance in automated methods for inspection, and monitoring of bulk tissue 3D spatial properties via robotically-directed sensing, which reduces the need for manual tissue handling and requirement for sensor-product interface prior to characterization.

#### II. MATERIALS AND METHODS

#### A. Materials

Lead zirconate titanate (PZT-5A; 72.4 × 72.4 × 0.127 mm³) with nickel electrodes was purchased from Piezosystems (Woburn, MA). Borosilicate glass was purchased from VWR. Glass cylinders and ethanol (200 proof) were from Fisher Scientific. Polyurethane (Fast-Drying) was from Minwax. Epoxy (EA 1C-LV) and cyanoacrylate (409 Super Bonder) were from Loctite. Polycarbonate (PC) film was from Laminated Plastics. Copper wires (16 gauge) and polyvinylidene fluoride were from McMaster-Carr. 5-minute epoxy was from Devcon. Dichloromethane was purchased from Sigma-Aldrich. Ultrapure deionized water (DIW) was from a commercially-available DIW system (Direct-Q 3UV; Millipore). Polylactic acid (PLA) filament was purchased from LulzBot. Pluronic F-127 (PF127) was from MilliporeSigma. Silicone (SI 595 CL) was from Loctite.

#### B. Sensor Fabrication

Piezoelectric-excited millimeter cantilever (PEMC) sensors and multifunctional fiber impedimetric sensors were selected for spatiotemporal sensing of animal and plant tissue mechanical properties and bioimpedance characteristics (e.g., dielectric property), respectively. PEMC sensors were fabricated from lead zirconate titanate (PZT) and borosilicate as described in previous studies [38], [39]. The resulting PEMC sensor exhibited a rectangular geometry of  $3 \times 1 \times 0.127 \text{ mm}^3$  (L-w-t), where L, w, and t represent the cantilever length, width, and thickness, respectively. Hollow multifunctional fibers were fabricated using PC films and copper wire as described in previous studies [14], [40]. The resulting hollow fiber sensors exhibited a cylindrical geometry with a diameter of 0.5 mm and a length of 20 mm The spacing between the embedded two copper electrodes was about 0.3 mm. Copper electrodes were exposed by a flat cutting at the sensing end. At the other end, 20-mm-long copper wires were exposed to serve as connecting leads by etching PC using dichloromethane. 5-min epoxy was applied at the connecting end to prevent contact between the two copper wires. While copper electrodes were used in this study, the electrode material in contact with the object can be subsequently modified, such as via physical vapor deposition. The sensing devices were affixed to a three-axis robot (MPS75SL; Aerotech) for the spatiotemporal biosensing process.

#### C. Measurement Principle and Data Acquisition

The resonant frequency  $(f_n)$ , phase angle at resonance  $(\phi_n)$ , and impedance  $(Z_n)$  at resonance of PEMC sensors were continuously monitored with a vector-network analyzer with

an impedance option (E5061b-005; Keysight). The sensor's dynamic mechanical response, here, the frequency response, was obtained via electromechanical coupling effects using electrical impedance analysis, which provides the electrical impedance magnitude (|Z|) and phase angle ( $\phi$ ) spectra of the piezoelectric layer (|Z| and  $\phi$  vs. frequency (f), respectively). Electrical impedance analysis was performed using a stimulus amplitude of 100 mV AC and zero DC bias across a frequency range  $f_n \pm 10$  kHz. Sensor signals ( $f_n$ ,  $\phi_n$ , and  $Z_n$ ) were acquired in real-time using a custom MATLAB program.

The impedance response of the multifunctional fiber sensors was monitored using a potentiostat (Interface 1010E, Gamry Instruments) using a two-electrode format. The two copper electrodes served as the working and counter electrode. The electrical impedance response of the system, which provides the electrical impedance magnitude (|Z|) and phase angle ( $\phi$ ), was obtained at 10 kHz using an AC voltage of 10 mV and zero DC offset with a sample time of 1 s. The fixed monitoring frequency (10 kHz) was selected as previous studies on bioimpedance analysis on tissues and cells suggest that the maximum relative difference is observed at 10-20 kHz [14], [41]. The object's tissue properties can subsequently be quantified via calibration (see Section I).

### D. Spatiotemporal Sensing Process Using Point Cloud-Based Path Planning

Previously reported point cloud-based path planning (PCPP) algorithm for non-planar 3D printing process [42] was modified to generate a collision-free path planning for inspection of free-form surfaces. The workflow of the proposed methodology consisted of three steps: point cloud generation, registration and preliminary path planning, and collision detection and corrections.

#### E. Point Cloud Generation

The point cloud generation process started by placing three user-defined reference points (~1 mm diameter) around the perimeter of the object using removable stickers or a black marker, or by placing the object on a pre-marked stage. The object was then scanned using a single camera-projector structured-light scanning system (HP 3D Structured Light Scanner Pro S2; HP) to acquire the point cloud data following our previously reported protocols [43], [44], [45], [46]. The objects were scanned by performing 1 to 4 scans over a 360° rotational angle to capture the surface geometry from various angles depending on the geometric complexity of the part. The point cloud data could be acquired in a single scan if it spans the required sensing area on the part and the reference points. The point cloud input to the algorithm is required to encompass the reference points, span the entire sensing domain, and have sufficient density to effectively represent the surface features. Later, the point cloud data was converted into a triangulated mesh file representing the surface topography of the object. The resulting mesh surface (S) was then transferred to the computer-aided design (CAD) software (Rhino 6), which here served as a platform for the implementation of the reverse engineering-driven tool path planning program.

#### F. Registration and Preliminary Conformal Path Planning

The developed algorithm was implemented using the Rhino-Script tool of Rhinoceros 6 software. 2D filled path was generated to encompass the sensing domain given by the user and placed above the point cloud representation of the object using a custom program implemented in Rhino 6. The userdefined filled path consisted of continuous lines and curves. The adapted PCPP program commenced with a registration process that aligned the mesh surface (S) and user-defined path to the robot's reference frame and then projected the user-defined planar path onto the mesh surface in the z-axis direction as described in the previous study [42]. The output of the registration step in the program was a tool path  $(T^a)$  on the mesh surface, scanning through the user-defined inspection area with a zigzag pattern, and reference frame-aligned mesh surface  $S^a$ . The pseudo-code is provided in Algorithm 1 of Supporting Information.

Following the registration and projection steps, inspection distance (h), safety distance (d), and sensing tool geometry were obtained from the user by the program. The inspection (i.e., measurement/characterization) points (M) on the freeform surface of the object were then generated by dividing the path curve  $(T^a)$  based on the inspection distance (h) given by the user (i.e., one inspection point per h). The inspection distance was set 2-5 mm throughout the study. The  $i^{th}$ point in **M** is denoted by  $m_i = (x_i, y_i, z_i)$  i = 1, 2, ..., l where  $l = |L_p/h| + 1$ . Next, the tool path curve  $(T^a)$  was discretized to generate motion commands capable of resolving the path, resulting in an array of tool path points, T. The path density was determined by the metric of two path points per sensing tool width (w). The  $j^{th}$  point on **T** is denoted by  $p_i = (x_i, y_i, y_i, y_i)$  $(z_j)$  j=1,2,...,k where  $k=|2L_p/w|+1$ , where  $L_p$  is the total length of the user-defined path (i.e., k points along the path). In this study, the width of the cantilever sensor was taken as the length of its longest edge (1 mm), and the width of the fiber sensor as its diameter (0.5 mm). The path points in T were then offset from the surface along the z-axis direction by a safety distance d given by the user. The safety distance d was set as 2 mm throughout the study since it is usually determined as 2 - 5 mm in contact-based inspection studies [32]. However, the proposed algorithm is capable of generating collision-free conformal path planning for a safety distance as small as 0.6 mm as shown in a previous study [42]. The output of this step of the program is the preliminary tool path points T and the inspection points M (i.e., measurement/characterization locations).

#### G. Conformal Path Planning

Given that the inspection process requires conformal path planning, the program runs a collision detection and correction step based on the surface features of the object and the sensing tool geometry. If a collision is detected, the path points in  $\mathbf{T}$  are offset from the surface by modifying the x- and y-axis coordinates to avoid a collision. Specifically, the path planning program utilizes the mesh surface representing the surface topography ( $S^a$ ), the tool path points ( $\mathbf{T}$ ), the sensing tool geometry as input parameters, and outputs collision-free path

points conforming to the free-form surface  $(p_j, p_{j+1},...,p_{j+n})$ that connects two consecutive inspection points  $(m_i \text{ and } m_{i+1})$ , where n = 2h/w. This part of the program started by determining the infeasible inspection points (i.e., locations) that cannot be reached by the sensing tool whose workspace is constrained by the tool geometry and the 3-axis cartesian robot. Two polysurfaces G and Q was generated to simulate the tool and tool holder geometry, respectively by the program. The center of the tool tip was positioned at each inspection point  $m_i$  to examine if there is an intersection between the tool holder geometry  $(Q_i)$  and the mesh surface  $(S^a)$  representing the object geometry. Thus, if the program detected a potential tool-surface collision at a given inspection point, that point  $m_i$  was removed from the feasible inspection points array M. To ensure contact between the sensor and the surface at the inspection points, the feasible inspection points  $(m_i)$  were offset towards the object by 0.5 mm in the z-axis direction. Next, potential collisions were detected across the tool path points in T. Similar to the infeasibility detection method, the tool geometry (G) was positioned along the path to simulate the tool motion in a way that the center of the tool tip was placed at each  $p_i$  in **T** to detect interference between the tool  $(G_i)$  and the object surface  $(S^a)$ . If the program detected a potential collision at a path point  $p_i$ , then the path point was moved laterally away from the surface by  $L_i$  in the direction of  $-V_i$  to avoid interference between the tool and the surface.  $L_i$  was calculated as the distance to achieve a lateral safety gap of 0.1 mm between the closest points on the surface and the tool.

$$V_j = \overrightarrow{p_j, c_j} \tag{1}$$

$$r_{j} = |p_{j}, q_{j}|, q_{j} \in \{G_{j} \cap \overline{p_{j} + MV_{j}}\}$$

$$(2)$$

$$L_i = r_i - |p_i, c_i| + 0.1 (3)$$

where  $c_j$  is the centroid of the intersection points list  $\{G_j \cap S^a\}$ , and M is a number greater than the tool width w. The corrected path points in T were calculated based on two cases determined by the tool-object intersection:

**Case1:** There exists no intersection between  $G_i$  and  $S^a$ .

$$p_j = p_j \tag{4}$$

Case2: There exists an intersection between  $G_i$  and  $S^a$ .

$$p_i = p_i + L_i V_i \tag{5}$$

The pseudo-code is provided in Algorithm 2 of Supporting Information and the flowchart of the overall methodology is provided in Fig. 1f. The output of the program was a collision-free conformal path planning for spatiotemporal sensing, including the inspection points  $\mathbf{M}$  and travel points between the inspection points  $\mathbf{T}$ . For a collision-free path from  $m_i$  to  $m_{i+1}$ , the tool follows the path  $p_j \rightarrow m_i \rightarrow p_j \rightarrow p_{j+1} \rightarrow \ldots \rightarrow p_{j+n} \rightarrow m_{i+1} \rightarrow p_{j+n}$  and waits t seconds at each inspection point to collect the sensor response. The wait time t was set as 15 seconds for both PEMC and fiber sensors since sensor response takes approximately 15 seconds to stabilize at the inspection points. The adapted PCPP program outputs a g-code (e.g.,  $GO1 \times X_1 \times Y_1 \times Z_1$ ) as motion control data describing the resulting path planning.

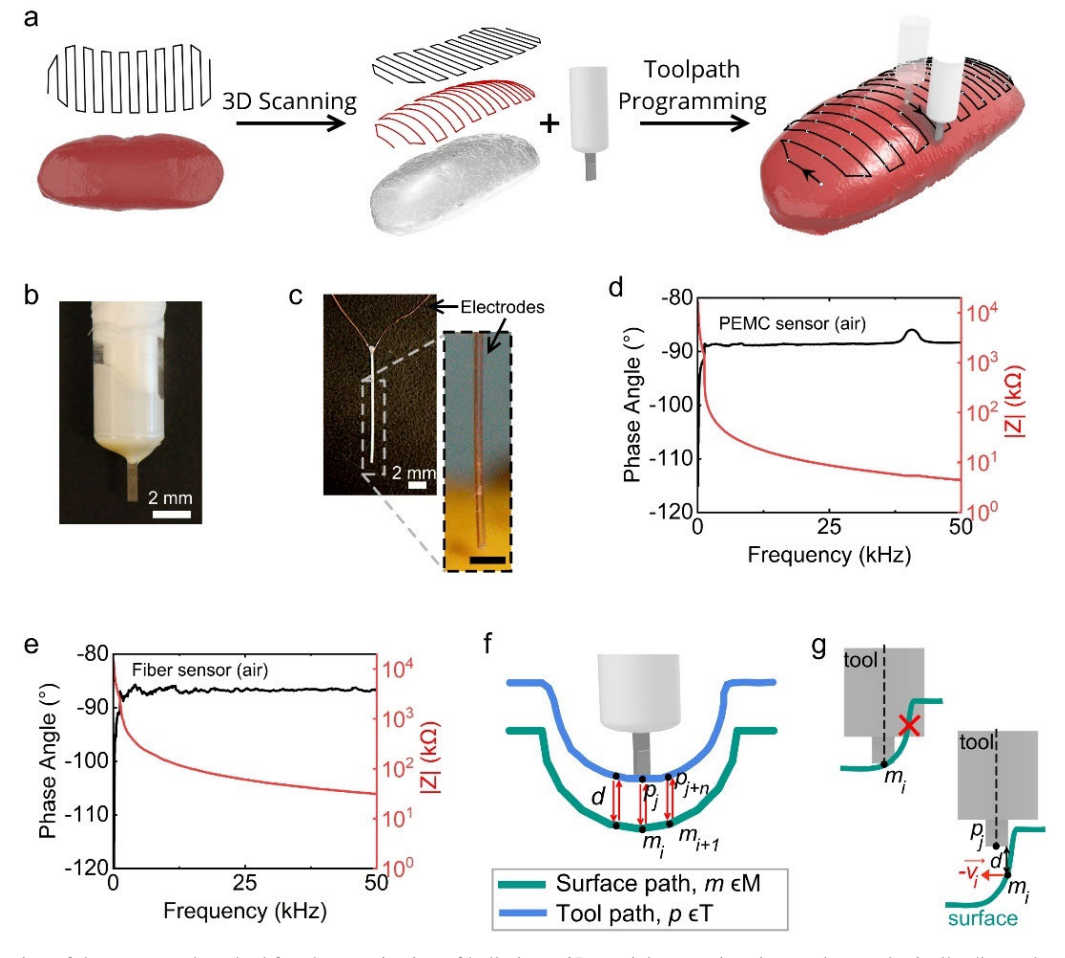


Fig. 1. (a) Illustration of the automated method for characterization of bulk tissue 3D spatial properties via nonplanar robotically-directed sensing. Photographs of the piezoelectric-excited millimeter cantilever (PEMC) (b) and multifunctional fiber (c) impedimetric sensors. Phase angle and impedance spectrum of the PEMC sensor (d) and the fiber sensor (e) over the frequency range of 5 Hz-50 kHz in air. Illustration of the nonplanar inspection path generated by the adapted PCPP nonplanar path planning algorithm (f) and tissue collision mitigation principle (g). Scale bars = 2 mm.

#### H. Fabrication of the Spherical Test Part

The hemisphere test part (R = 20 mm, h = 15 mm) was created using CAD software (Rhino 6). The hemisphere part was selected for characterization of the spatiotemporal sensing algorithm since the spherical surfaces exhibit challenging topographical features for conformal path planning [47]. The test part was fabricated using a plastic extrusion 3D printer (Mini2; LulzBot) with vendor-recommended settings. Briefly, a linear velocity of 60 mm/s, layer spacing of 0.18 mm, and gradual infill density ranging from 10% to 90% were used to fabricate the test part. Next, Pluronic F127 hydrogel (30 wt%) and RTV silicone were conformally printed following a circular filled pattern using the adapted PCPP algorithm across the surface of the test part with a 20-gauge tapered tip (d = 0.6 mm), extrusion pressure range of 8-15 psi, and printing speed of 5 mm/s. The conformal 3D printing was performed using a custom microextrusion 3D printing system, which included a three-axis robot (MPS75SL; Aerotech), a digital pressure regulator (Ultimus V; Nordson), and a motion controller (A3200; Aerotech).

#### I. Characterization of Test Part and Tissue Properties

The proposed methodology was applied to characterize a test part and multiple foods, including animal and plant tissue.

(meat), and plant tissue (fruit). Food (meat - beef and fruit avocado) was obtained from a local grocer and maintained at room temperature for 1 h prior to characterization. The characterization process was completed on the objects using a 3-axis robotic system with a feed rate of 1 mm/s throughout the study. Prior to freezing-thawing treatment of the food (meat) samples, the bioimpedance distribution was first characterized at room temperature. The food samples were subsequently stored at -18° C for 24 hours and then at 4° C for 24 hours. The sample was then maintained at room temperature for 1 hour prior to characterization. The total inspection time was 25 seconds per inspection point. The temporal resolution of the system is determined by the sensing tool's sampling rate and stabilization time. The PEMC sensor response to contact with samples of varying Young's modulus was calibrated by micro-indentation studies on polydimethylsiloxane (PDMS) standards [48]. The sensor signals were continuously recorded during the calibration process. The signals were first allowed to stabilize with the PEMC sensor positioned above the surface of the PDMS standard (formed in a single well of a standard 6-well plate). The sensor was then lowered at a constant rate using a manual micromanipulator until sample contact, which was identified as the position at which the PEMC sensor signal underwent a change greater than 10 times the

signal-to-noise ratio. This initial contact position was referred to as the position associated with zero strain. The sensor signals were then allowed to stabilize. The sensor response was then continuously recorded as the penetration depth underwent several step changes. Neglecting the thickness of the PEMC coating, the microcontact area for the PEMC sensor was  $wt(0.127 \text{ mm}^2)$ .

#### J. Data Analysis and Image Processing

The sensor signals were continuously recorded during the spatiotemporal sensing process. Thus, the sensor data at the inspection points (i.e., when the sensor was in contact with the object) was isolated from the sensor data in air (i.e., when the sensor was traveling to the next inspection point) using the peak analyzer in Origin Pro 2021, and the average sensor response was recorded for each inspection point. The sensor response could not be recorded when the sensor failed to be in contact with the sample. Hence, the sensor response data was matched with the inspection points using the timestamps. The inspection points on the test part were next categorized as Pluronic F127 hydrogel and silicone based on the corresponding material type at that point using image analysis. Similarly, the points on the animal tissue were labeled as muscle and adipose tissue. Photographs of the tissue were acquired by using a digital camera (D7200; Nikon) from the top view before the spatiotemporal sensing process. The photographs were analyzed using image analysis software (ImageJ; NIH) and CAD software (Rhinoceros 6). The adipose tissue was first isolated using the 'color threshold' command to filter the white color associated with the adipose tissue. The filtered image was then transferred to CAD software along with the inspection points to detect the corresponding tissue type. The same process was applied to the test part to isolate the Silicone material using image analysis and to categorize the inspection points.

#### K. Statistical Analysis

Statistical analysis was completed in Origin Pro 2021. Student's or Welch's t-test was used for the experiments except for the before/after freezing the animal tissue experiment where paired t-test was used. \*, \*\*, and \*\*\* indicate a p-value (p) less than 0.05, 0.01, and 0.001, respectively. The number of inspection points (n) is specified for each experiment.

#### III. RESULTS AND DISCUSSION

A. Concept of Robotically-Directed Nonplanar Tissue Property Inspection via Real-Time Combinatorial Impedimetric Sensing

Monitoring of spatial distributions of tissue property is typically done using conforming sensor arrays, which requires manual integration of sensors with target tissue and continuous sensor-tissue contact. An automated robotically-directed sensing method offers the ability to choose dynamic sampling locations and have minimal impact on the surface of the tissue. As shown in Fig. 1, the automated method for characterization of bulk tissue and organ 3D spatial properties

begins with nonplanar toolpath generation for the roboticallydirected sensing process. A nonplanar inspection path was generated across the object (e.g., tissue) surface for PEMC and fiber sensors (see Fig. 1a-c) based on point cloud data to cover the user-defined inspection area and safety tolerance (d). PEMC sensors facilitate the characterization of hydrogel viscoelastic properties via electrical impedance spectroscopy and real-time monitoring of circuit (sensor) resonant frequency, quality factor, and phase angle across the 10 - 50 kHz frequency range [49], [50], [51]. Multifunctional fibers facilitate characterization of tissue bioimpedance via electrochemical impedance spectroscopy and real-time impedimetric monitoring of circuit (sensor) impedance at a fixed frequency (10 kHz) [14], [41], [52]. PEMC sensors and multifunctional fiber sensors have been used previously for long-term liquid-based and in vivo sensing studies. Thus, the sensors are attractive sensors for automated inspection of tissue properties. Phase angle and impedance spectrums of the PEMC and fiber sensors over the frequency range of 5 Hz - 50 kHz in air are provided in Fig. 1d and e, respectively. An illustration of the inspection path generated by the adapted PCPP algorithm is shown in Fig. 1f and g, which avoids potential tissue damage via tool collision. A description of the adapted PCPP algorithm for tissue inspection path generation is also provided in Fig. 2.

# B. Validation of the Automated Method for Characterization of Bulk Tissue 3D Spatial Mechanical Properties Using a Test Part

Having described the measurement principle, we next validated the method by characterization of 3D test parts that exhibited varying spatial distributions of tissue property. To establish a 3D test part that exhibited a distribution of mechanical properties, patterns of hydrogel and silicone were printed onto a 3D test part. The materials in the regions from the inner circle through the outer circle were hydrogel, silicone, and hydrogel, respectively (Fig. 3a and b). The inspection path corresponding to a distance of 2 mm between adjacent inspection (i.e., measurement/characterization) points is shown in Fig. 3a and b. Fig. 3c shows the representative temporal PEMC sensor resonant frequency and phase angle responses for three measurement events. The spatial distribution of the sensor response at each measurement location is obtained based on the known relationship between measurement time and tool path location. The ability of the PEMC sensor to detect the stiffness of the sample through microcontact measurement is shown in Fig. 3d. Fig. 3e shows the 3D spatial distribution of the PEMC sensor phase angle response across the test part from a top-down perspective. Fig. 3f and g highlight the 3D spatial distributions of the PEMC sensor phase angle and resonant frequency responses, responses, respectively. The material type corresponding to each inspection point obtained using image analysis is also highlighted in Fig. 3h. As shown in

Fig. 3i, the phase angle of the sensor in Pluronic F127 hydrogel (n=85 inspection points) was significantly different than the phase angle in silicone (n=94 inspection points) (p<0.001), which has a significantly lower

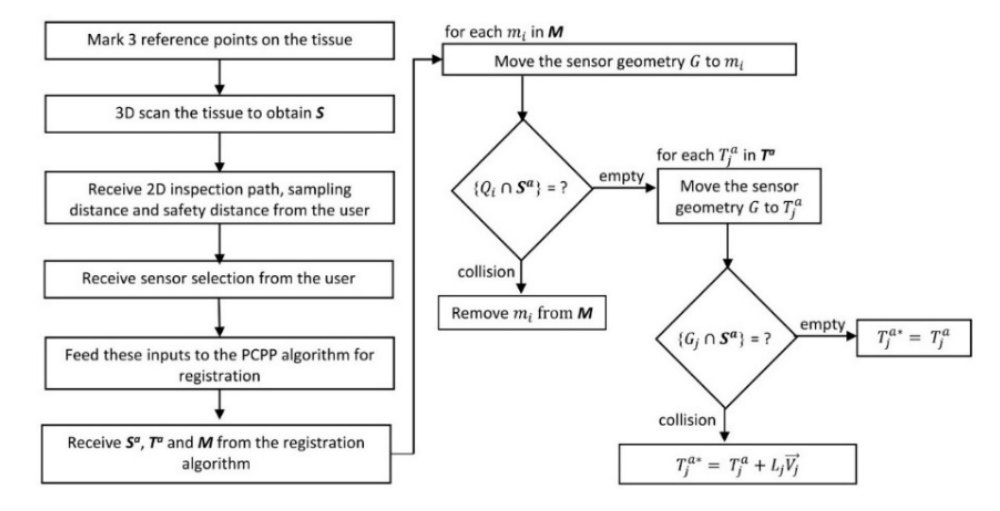


Fig. 2. Description of the adapted PCPP program for nonplanar inspection path generation.

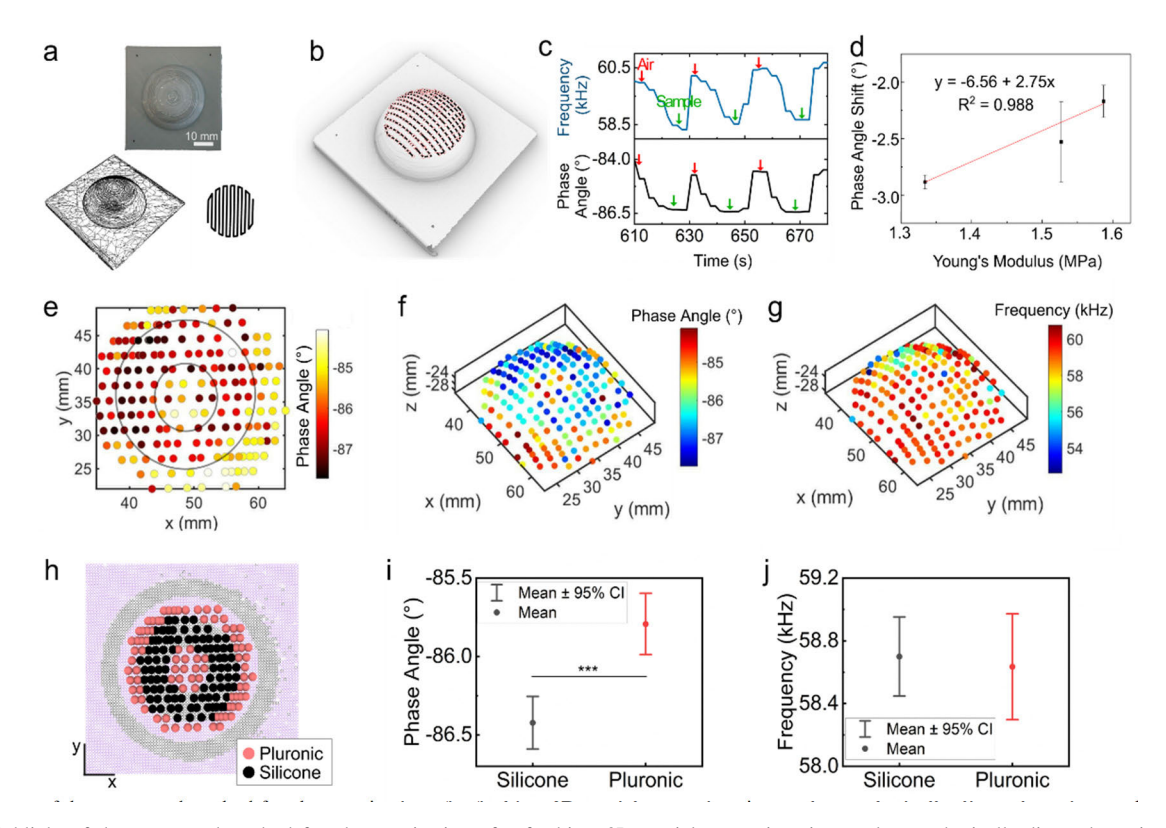


Fig. 3. Highlight of the automated method for characterization of soft object 3D spatial properties via nonplanar robotically-directed sensing on the test part with a spherical surface. a) Photograph and associated scanning data. b) Rendered projected tool path data onto point cloud data. c) Partial time-series data showing the observed cantilever impedance phase angle and resonant frequency as the tool travels through the inspection points collecting data in air and on the sample. d) Calibration of PEMC sensor for characterization of material Young's modulus via microcontact measurement using PDMS standards. e) 2D spatial distribution of phase angle at the inspection points on the object. 3D spatial map of the phase angle (f) and the resonant frequency (g) across the object. h) 2D map of the material types corresponding to each inspection point. Comparison of the phase angle (i) and the resonant frequency (j) of the cantilever sensor on Silicone and Pluronic F127. (\*\*\*p < 0.001).

modulus (0.02-0.03 vs. 1.6-4.1 MPa) [53], [54], [55]. The estimated boundaries between materials are highlighted in Fig. 3e. A comparison of the estimated boundaries with the part's 3D spatial distribution of properties is shown in Fig. 3h. We note that while the PEMC sensor phase angle response exhibited a significant correlation with the mechanical properties (Fig. 3j), the resonant frequency

response did not provide a direct correlation, which is consistent with previous studies. For example, the phase angle and the frequency changed from  $\phi = -85.79 \pm 0.96^{\circ}$  and  $f = 58.63 \pm 1.56$  kHz, respectively, to  $\phi = -86.42 \pm 0.82^{\circ}$  and  $f = 58.63 \pm 1.56$  kHz as the sensor moved from contact with Pluronic F127 (G' = 28.6 kPa) [56] to silicone (E = 0.44 MPa) [44].

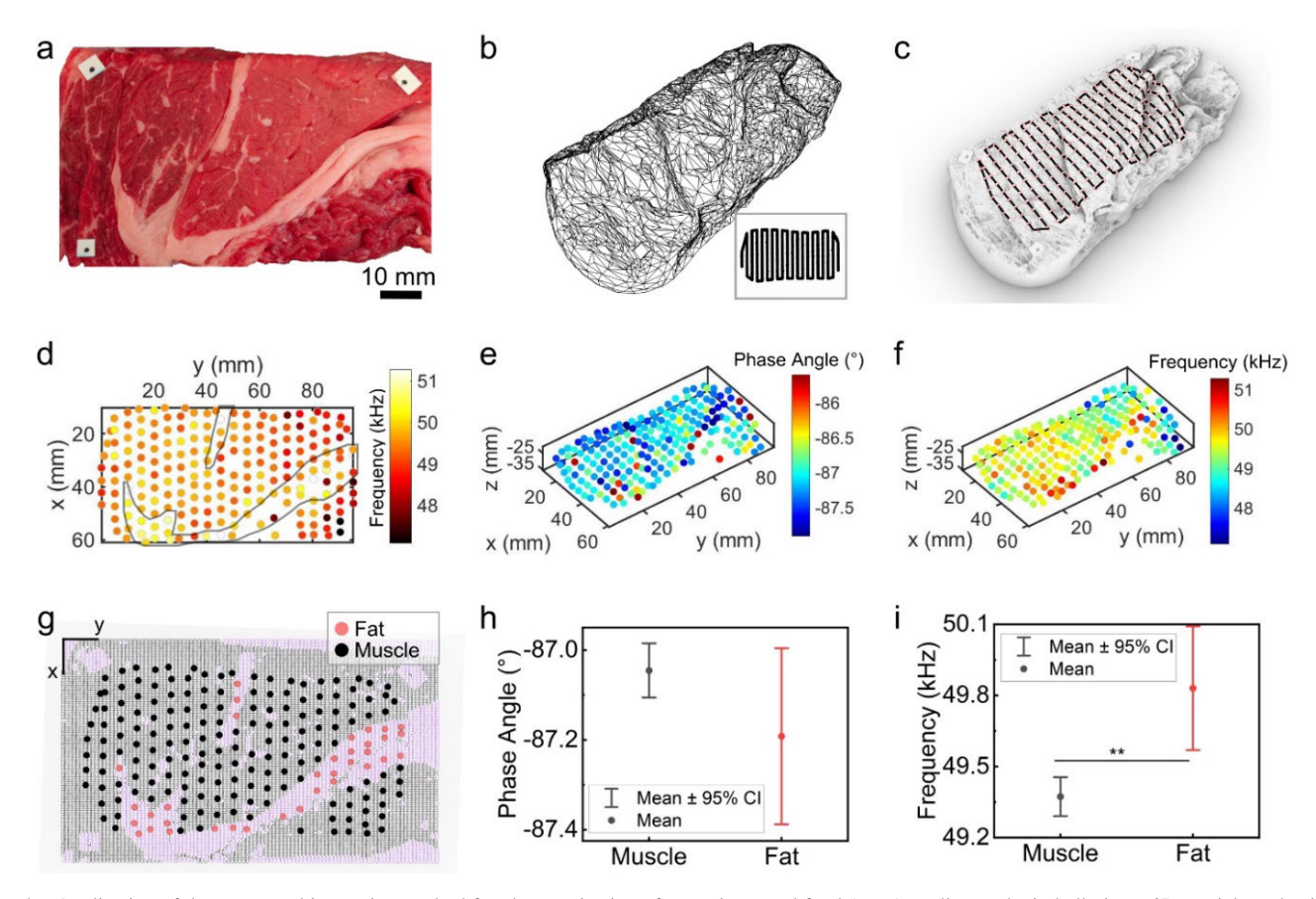


Fig. 4. Application of the automated inspection method for characterization of meat tissue and food (meat) quality to obtain bulk tissue 3D spatial mechanical properties via nonplanar robotically-directed sensing using PEMC sensors. Photograph (a) and associated scanning data (b) of the food sample (muscle tissue). (c) Rendered projected tool path data onto point cloud data. d) 2D spatial distribution of the resonant frequency of the cantilever sensor at the inspection points on the sample. 3D spatial map of the phase angle (e) and the resonant frequency (f) across the sample. g) 2D map of the tissue types corresponding to each inspection point. Comparison of the phase angle (h) and the resonant frequency (i) of the cantilever sensor on muscle and adipose tissue. (\*\*p < 0.01).

C. Automated Characterization of Muscle Tissue and Food (Meat) Quality (Adipose (Fat)-to-Muscle Tissue Distribution) via Robotically-Directed Conformal Sensing Using PEMC Sensors

Having demonstrated that the method enables mapping of the non-uniform mechanical property distribution of a test part that coincided with the non-uniform distribution of hydrogel and elastomer coatings, we next applied the method for characterizing the spatial distribution of mechanical and dielectric properties of natural tissues. The composition of meat products, such as the adipose tissue (fat) ratio, is recognized as being an important quality measure since adipose tissue carries an important contribution to the taste [17], [57], [58], [59]. The resulting adipose (fat)-to-muscle tissue ratio can be used as an estimator for the sensory quality of meat [17], [57], [58], [59]. The tool path associated with the nonplanar inspection of the meat sample is shown in Fig. 4a-c. The Young's modulus of adipose and muscle tissue has been previously characterized as 2-4 and 12-18 kPa, respectively [60], [61], [62]. Thus, the results associated with Fig. 3 suggest that the method may facilitate automated characterization of the adipose tissue distribution throughout the muscle tissue. Recall, our control studies shown in Fig. 3 show that robotically-directed sensing via PEMC sensors facilitates resolution of the 3D spatial distribution of a soft object's mechanical properties. The spatial

distributions of the phase angle and the resonant frequency of the PEMC sensor across the meat are presented in Fig. 4d-f (see Video S1). The estimated boundaries between the tissue contents are highlighted on the 2D property map of the meat in Fig. 4d. Fig. 4g shows the tissue type distribution on the inspection points. As shown in Fig. 4h and i, the difference in the PEMC sensor phase angle on muscle and adipose tissue was not significant, while the resonant frequency on muscle (n=170) inspection points) was significantly different than on adipose tissue (n=35) inspection points) (p=0.003)  $(\phi=-87.05\pm0.39^\circ$  and  $f=49.37\pm0.54$  kHz for muscle tissue vs.  $\phi=-87.19\pm0.57^\circ$  and  $f=49.83\pm0.76$  kHz for adipose tissue).

#### D. Automated Characterization of Plant Tissue and Food (Fruit) Quality (Ripeness) via Robotically-Directed Conformal Sensing Using PEMC Sensors

Having applied the method to automated characterization of bulk muscle tissues that exhibit a variation of surface height across a 44 cm<sup>2</sup> area, we next applied the method to characterization of bulk plant tissues that exhibit increasingly complex shape. Several studies show that the changes in the mechanical properties and electrical impedance of fruits are correlated with the physiological state of the fruits such as apples, bananas, and avocados [22], [63], [64], [65], [66], [67].

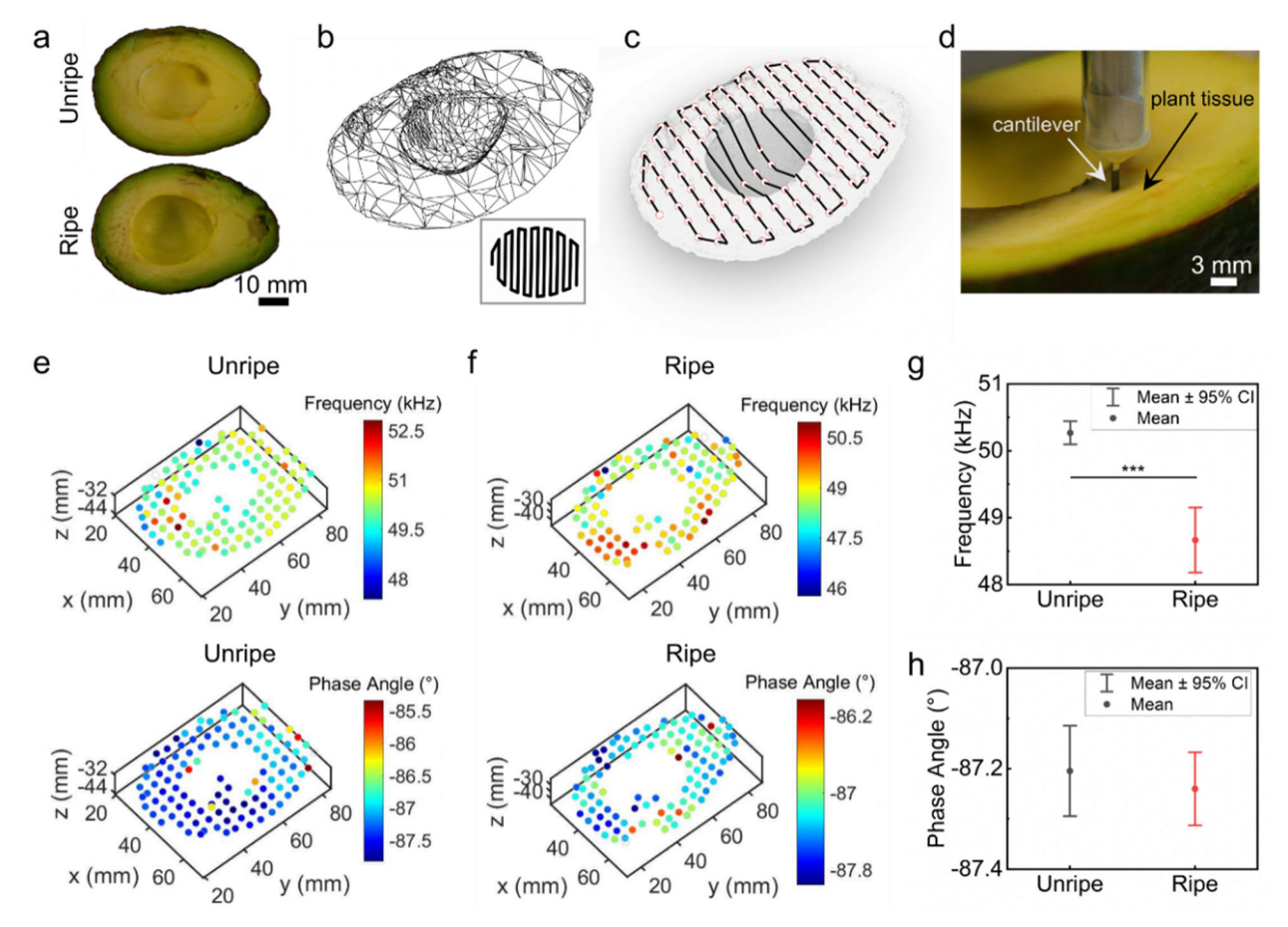


Fig. 5. Application of the automated inspection method for characterization of plant tissue and food quality (fruit ripeness) to obtain bulk tissue 3D spatial mechanical properties via nonplanar robotically-directed sensing using PEMC sensors. Photograph (a) and associated scanning data (b) of the fruit sample (avocado). c) Rendered projected tool path data onto point cloud data. d) Photograph showing the PEMC sensor at an inspection point on the fruit during the characterization process. 3D spatial map of the resonant frequency and phase angle across the unripe (e) and ripe fruit (f). Comparison of the resonant frequency (g) and the phase angle (h) of the cantilever sensor across the unripe and ripe fruit. (\*\*\*p < 0.001).

Fig. 5a-d show the application of the automated process for spatial tissue property inspection to characterization of fruit quality, specifically, the ripeness of avocados. Fig. 5e and f show the spatial distribution of the PEMC sensor resonant frequency and phase angle across the unripe and ripe avocado, respectively. While the change in phase angle response between the unripe and ripe samples was insignificant, as shown in Fig. 5g-h, the resonant frequency of the PEMC sensor on the unripe avocado (n = 114 inspection points;  $f = 50.27 \pm 0.93$  kHz) was significantly different than on the ripe avocado (n = 103 inspection points;  $f = 48.67 \pm 2.49$  kHz) (p < 0.001).

E. Automated Characterization of Muscle Tissue and Food (Meat) Quality (Bioimpedance Distribution) via Robotically-Directed Conformal Sensing Using Multifunctional Fiber Sensors

Having established that PEMC sensors facilitate automated characterization of bulk tissue 3D spatial mechanical properties of multiple tissue and food types, we next examined the ability to characterize additional bulk properties via alternative sensor selection, such as multifunctional fibers (see Fig. 1). Fig. 6a-d show application of the method to characterization of meat quality via automated mapping 3D spatial bioimpedance

distribution using multifunctional fiber sensors. The electrical impedance of meat (i.e., bioimpedance) can be utilized as a freshness indicator in quality control, since freezing and thawing of meat disrupts cellular structure because of ice crystal formation [17], [68]. Hence, freezing processes impact the dielectric properties of composite tissues, such as meat [25]. Bioimpedance analysis has also been used to characterize the adipose tissue (fat) composition in meat products given that the water content and dielectric properties differ in muscle and adipose tissues [17], [57]. The spatial distributions of the tissue impedance (i.e., bioimpedance) at 10 kHz and phase angle based on the multifunctional fiber sensor before and after the freeze-thaw cycle are shown in Fig. 6e and f, respectively (see Video S2). Fig. 6g shows that the meat exhibited a higher bioimpedance after freezing-thawing treatment than before the freezing. The bioimpedance was significantly different on the meat before (n = 167 inspection points) and after (n = 167 inspection points)167 inspection points) ( $|Z| = 0.13 \pm 0.09 \text{ M}\Omega \text{ vs. } |Z| =$  $0.25 \pm 0.08 \text{ M}\Omega$ , respectively; p < 0.001). The difference in phase angle before and after the temperature treatment was not significant.

Similar to the tissue type characterization using the cantilever sensor (Fig. 3), we also examined whether the phase angle and impedance are significantly different on adipose

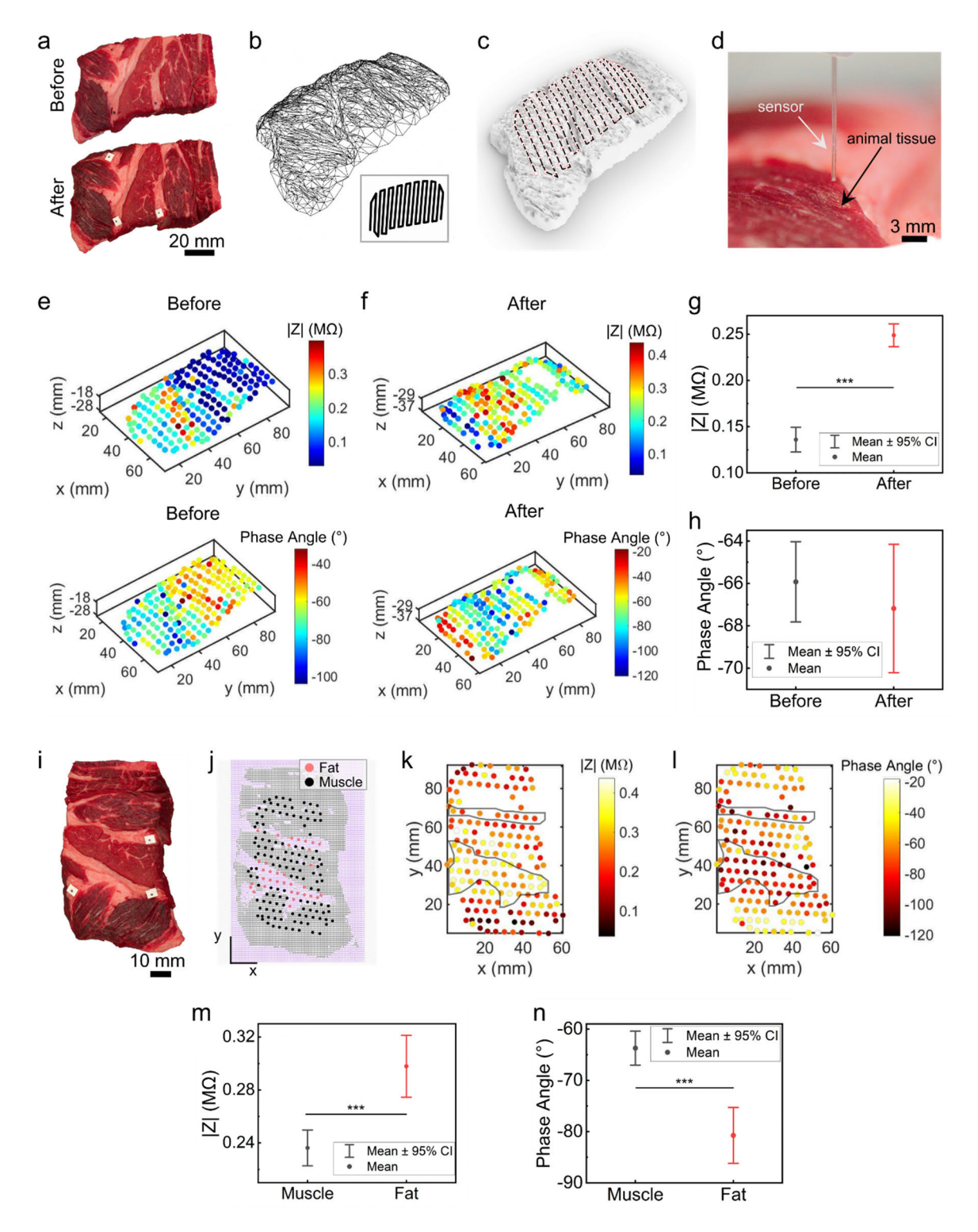


Fig. 6. Application of the automated inspection method for characterization of meat tissue and food quality (meat freshness) to obtain bulk tissue 3D spatial mechanical properties via nonplanar robotically-directed sensing using multifunctional fiber sensors. Photograph (a) and associated scanning data (b) of the meat. (c) Rendered projected tool path data onto point cloud data. (d) Photograph showing the fiber sensor above an inspection point on the meat during the spatiotemporal sensing process. 3D spatial map of the impedance and phase angle before (e) and after (f) freezing and thawing of the meat. Comparison of the impedance (g) and the phase angle (h) of the fiber sensor across the meat before and after freezing and thawing. (\*\*\*p < 0.001). (i) Photograph of the meat. (j) 2D map of the tissue types corresponding to each inspection point. 2D spatial distribution of the impedance (k) and phase angle (l) of the fiber sensor at the inspection points on the meat. Comparison of the impedance (m) and the phase angle (n) of the fiber sensor on muscle and adipose tissue. (\*\*\*p < 0.001).

and muscle tissue after freezing and thawing using the data the meat and tissue types obtained by image processing on shown in Fig. 6f. Fig. 6i and j show the top view of the inspection points, respectively. Fig. 6k and 1 show 2D

spatial property maps for impedance and phase angle across the meat, respectively. The estimated boundaries between the tissue types are highlighted in Fig. 6k and l. As shown in Fig. 6m and n, the impedance and phase angle on muscle (n=133 inspection points) were significantly different than on adipose tissue (n=34 inspection points) (p<0.001). Specifically, the sensor exhibited an impedance and phase angle of  $|Z|=0.24\pm0.08$  M $\Omega$  and  $\phi=-63.72\pm19.34^\circ$ , respectively, on muscle tissue, while it exhibited  $|Z|=0.30\pm0.07$  M $\Omega$  and  $\phi=-80.73\pm15.59^\circ$  on adipose tissue.

In summary, this study was motivated by the need for creating new methods for inspecting the material properties of soft objects, such as biomanufactured and natural tissues (e.g., connective tissue or food) or organs, without the need for placing fixed measurement devices on the object (e.g., using a conforming wearable sensor or sensor array). However, the current inspection methods for soft objects are traditionally based on non-contact image analysis, which may or may not involve path planning, or wearable sensors (e.g., conforming sensor arrays) that are fixed to the object. While imagebased methods may provide indirect characterization of some material properties and performance-quality characteristics, contact-based sensing modalities provide expanded opportunities to interrogate material properties. While wearable sensors provide a useful form factor, wearable sensing can pose challenges associated with sensor-object interactions and flexibility in measurement location if the application involves a case where maintained integration of the sensor may affect the object quality (e.g., tissue quality) or function. The knowledge gap that impedes overcoming these challenges of inspecting soft objects and spatially monitoring the material properties of soft objects is the lack of understanding for how the design characteristics and transduction mechanisms of contactbased material property sensors can inform non-planar path planning algorithms. The aim of this study was to create and validate an automated method for characterizing the spatial distribution of a soft 3D object's material properties in two common sensor form factors (e.g., cantilever- and fiber-based contact sensors). Accomplishing this aim required creating a non-planar path planning method for milli- to micro-scale contact-based property sensors, which required establishing new path planning parameters driven by object geometry, sensor geometry, and the transduction mechanism of the sensor. Given the extensive use of 3D scanning in biomedical-oriented reverse engineering applications, we adapted a non-planar path planning method based on structured-light scanning that was initially created for conformal additive manufacturing applications by introducing new path planning parameters based on the design, transduction mechanism, and measurement requirements of sensor-based measurement tools for material property characterization.

The contributions (i.e., advantages) of this method stem from the use of a robotically-directed sensing principle and reverse engineering-driven path planning method. While the use of wearable sensors or conformal sensor arrays for material property sensing require placement on the object, and often fixation to the object, this method avoids the need for sensor placement and fixation to the object. Thus, it can address

challenges associated with sensor placement on soft objects, such as associated with mechanical mismatch or damaged caused by sensor removal. Another advantage of this method based on robotically-directed sensing using non-planar path planning arises from the flexibility offered in the sensing location. For example, the spatial distribution of inspection locations (i.e., spatial resolution) associated with wearable sensors or conformal sensor arrays is fixed following fabrication and placement and fixation to the object. In addition, the spatial resolution is determined by the design of the sensor array (e.g., spacing of array elements). In contrast, the spatial resolution for property inspection using this method is based on the performance of the motion control system (e.g., precision and accuracy) and selected path planning parameters, which can be rapidly tuned and modified to achieve alternative sensing locations or spatial resolution of measured properties. Given the ability to avoid need for sensor placement on objects and achieve high spatial resolution of property inspection based on the robotically-directed sensing and flexibility in rapid tuning and control of the measurement locations via path planning, this method has advantages in inspection applications that involving moving (e.g., deforming) soft objects. For example, the path planning method only requires time associated with point cloud data acquisition and processing (e.g., registration, if required) and computational time for the point cloud-based path planning algorithm, [42] which means that the tool path could be potentially updated prior to moving the sensor to the next measurement location.

The path planning algorithm could potentially be improved by incorporating feedback from the contact pressure of the sensor during sensing. In addition, the method can also be improved by use of a five-axis robot that would allow for improved control of the sensor-object contact angle during inspection. Adhesion between materials that may be on the surface of the soft object and sensor components may also lead to irreversible changes in the sensor signal that may require in situ sensor cleaning or replacement. Inspection of reflective or transparent soft objects may also pose a challenge to the method associated with acquisition of point cloud data, which is the driver to the point cloud-based path planning method. Object movement during inspection may also pose a challenge, but could be mitigated by running the point cloud-based path planning method in a closed loop [69].

#### IV. CONCLUSION

This work presented an automated method for characterizing the spatial distribution of material properties of non-planar macroscale tissues. Importantly, the method facilitates automated inspection of spatial tissue quality without the need for manual or prolonged sensor-tissue integration. The utility and impact of the method was validated by application to automated inspection of food quality based on the use of multiple impedimetric sensors that facilitate monitoring complementary tissue quality attributes, including 3D spatial distribution of mechanical properties and bioimpedance.

Here, we reported a novel method based on reverse engineering-driven non-planar path planning and roboticallydirected sensing for automated inspection of 3D spatial material property distributions. This method is potentially useful for automated inspection of foods and tissue-based products, such as additively manufactured implantable and consumable tissues and organs. Future studies may focus on developing closed-loop controlled inspection system by integrating displacement or pressure sensor feedback into the proposed conformal sensing methodology to ensure both sensor-tissue contact and constant contact pressure. Closed-loop controlled inspection systems may enable sensing on tissues and organs that are challenging for the 3D scanning process [69].

#### REFERENCES

- G. R. D. Prabhu and P. L. Urban, "The dawn of unmanned analytical laboratories," *TrAC Trends Anal. Chem.*, vol. 88, pp. 41–52, Mar. 2017, doi: 10.1016/j.trac.2016.12.011.
- [2] T. Brosnan and D.-W. Sun, "Improving quality inspection of food products by computer vision—A review," J. Food Eng., vol. 61, no. 1, pp. 3–16, 2004, doi: 10.1016/S0260-8774(03)00183-3.
- [3] G. Schneider, "Automating drug discovery," Nature Rev. Drug Discovery, vol. 17, no. 2, pp. 97–113, Feb. 2018, doi: 10.1038/nrd.2017.232.
- [4] H. Miller, Z. Zhou, J. Shepherd, A. J. M. Wollman, and M. C. Leake, "Single-molecule techniques in biophysics: A review of the progress in methods and applications," *Rep. Prog. Phys.*, vol. 81, no. 2, Feb. 2018, Art. no. 024601, doi: 10.1088/1361-6633/aa8a02.
- [5] M. Dey and I. T. Ozbolat, "3D bioprinting of cells, tissues and organs," Sci. Rep., vol. 10, no. 1, p. 14023, Aug. 2020, doi: 10.1038/s41598-020-70086-v
- [6] W. L. Ng, C. K. Chua, and Y.-F. Shen, "Print me an organ! Why we are not there yet," *Prog. Polym. Sci.*, vol. 97, Oct. 2019, Art. no. 101145, doi: 10.1016/j.progpolymsci.2019.101145.
- [7] H. Piwoński, Y. Wang, W. Li, T. Michinobu, and S. Habuchi, "Millimeter-deep detection of single shortwave-infrared-emitting polymer dots through turbid media," *Nano Lett.*, vol. 20, no. 12, pp. 8803–8810, Dec. 2020, doi: 10.1021/acs.nanolett.0c03675.
- [8] P. R. Coulet and L. J. Blum, Biosensor Principles and Applications. Boca Raton, FL, USA: CRC Press, 2019.
- [9] G. Rong, S. R. Corrie, and H. A. Clark, "In vivo biosensing: Progress and perspectives," ACS Sensors, vol. 2, no. 3, pp. 327–338, Mar. 2017, doi: 10.1021/acssensors.6b00834.
- [10] S. Vigneshvar, C. C. Sudhakumari, B. Senthilkumaran, and H. Prakash, "Recent advances in biosensor technology for potential applications—An overview," *Frontiers Bioeng. Biotechnol.*, vol. 4, pp. 1–10, Feb. 2016. [Online]. Available: https://www.frontiersin.org/ article/10.3389/fbioe.2016.00011
- [11] F. David, M. Hebeisen, G. Schade, E. Franco-Lara, and M. Di Berardino, "Viability and membrane potential analysis of *Bacillus megaterium* cells by impedance flow cytometry," *Biotechnol. Bioeng.*, vol. 109, no. 2, pp. 483–492, Feb. 2012, doi: 10.1002/bit.23345.
- [12] S. Gawad, L. Schild, and P. H. Renaud, "Micromachined impedance spectroscopy flow cytometer for cell analysis and particle sizing," *Lab Chip*, vol. 1, no. 1, pp. 76–82, 2001, doi: 10.1039/B103933B.
- [13] M. Angstmann, I. Brinkmann, K. Bieback, D. Breitkreutz, and C. Maercker, "Monitoring human mesenchymal stromal cell differentiation by electrochemical impedance sensing," *Cytotherapy*, vol. 13, no. 9, pp. 1074–1089, Oct. 2011, doi: 10.3109/14653249.2011.584863.
- [14] A. P. Haring et al., "3D bioprinting using hollow multifunctional fiber impedimetric sensors," *Biofabrication*, vol. 12, no. 3, Jul. 2020, Art. no. 035026, doi: 10.1088/1758-5090/ab94d0.
- [15] K. F. Lei, Z.-M. Wu, and C.-H. Huang, "Impedimetric quantification of the formation process and the chemosensitivity of cancer cell colonies suspended in 3D environment," *Biosensors Bioelectron.*, vol. 74, pp. 878–885, Dec. 2015, doi: 10.1016/j.bios.2015.07.060.
- [16] M. Genescà et al., "Electrical bioimpedance measurement during hypothermic rat kidney preservation for assessing ischemic injury," *Biosensors Bioelectron.*, vol. 20, no. 9, pp. 1866–1871, Mar. 2005, doi: 10.1016/j.bios.2004.06.038.
- [17] U. Pliquett, "Bioimpedance: A review for food processing," Food Eng. Rev., vol. 2, no. 2, pp. 74–94, Jun. 2010.
- [18] L. M. Ricles, J. C. Coburn, M. Di Prima, and S. S. Oh, "Regulating 3D-printed medical products," *Sci. Transl. Med.*, vol. 10, no. 461, Oct. 2018, Art. no. eaan6521, doi: 10.1126/scitranslmed.aan6521.

- [19] S. V. Murphy, P. De Coppi, and A. Atala, "Opportunities and challenges of translational 3D bioprinting," *Nature Biomed. Eng.*, vol. 4, no. 4, pp. 370–380, Nov. 2019, doi: 10.1038/s41551-019-0471-7.
- [20] A. O. Ojo et al., "Organ donation and utilization in the USA," Amer. J. Transplantation, vol. 4, pp. 27–37, Apr. 2004, doi: 10.1111/j.1600-6135.2004.00396.x.
- [21] D. El Khaled, N. N. Castellano, J. A. Gazquez, R. M. G. Salvador, and F. Manzano-Agugliaro, "Cleaner quality control system using bioimpedance methods: A review for fruits and vegetables," *J. Cleaner Prod.*, vol. 140, pp. 1749–1762, Jan. 2017, doi: 10.1016/j.jclepro.2015.10.096.
- [22] P. Ibba, A. Falco, B. D. Abera, G. Cantarella, L. Petti, and P. Lugli, "Bio-impedance and circuit parameters: An analysis for tracking fruit ripening," *Postharvest Biol. Technol.*, vol. 159, Jan. 2020, Art. no. 110978, doi: 10.1016/j.postharvbio.2019.110978.
- [23] A. Chowdhury, T. K. Bera, D. Ghoshal, and B. Chakraborty, "Studying the electrical impedance variations in banana ripening using electrical impedance spectroscopy (EIS)," in *Proc. 3rd Int. Conf. Comput., Commun., Control Inf. Technol. (C3IT)*, Feb. 2015, pp. 1–4, doi: 10.1109/C3IT.2015.7060196.
- [24] T. Yovcheva, E. Vozáry, I. Bodurov, A. Viraneva, M. Marudova, and G. Exner, "Investigation of apples aging by electric impedance spectroscopy," *Bulg. Chem. Commun.*, vol. 45, pp. 68–72, Jan. 2013.
- [25] M. A. Mousa, A. AboBakr, L. A. Said, A. H. Madian, A. S. Elwakil, and A. G. Radwan, "Heating and freezing injury to plant tissues and their effect on bioimpedance: Experimental study," in *Proc. 4th Int. Conf. Adv. Comput. Tools Eng. Appl. (ACTEA)*, Jul. 2019, pp. 1–4, doi: 10.1109/ACTEA.2019.8851098.
- [26] T. Yoshimoto-Haramura et al., "A simple rapid method for measuring liver steatosis using bioelectrical impedance," Vivo, vol. 36, no. 2, pp. 570–575, Mar. 2022, doi: 10.21873/invivo.12739.
- [27] M. Schwarz, M. Jendrusch, and I. Constantinou, "Spatially resolved electrical impedance methods for cell and particle characterization," *Electrophoresis*, vol. 41, nos. 1–2, pp. 65–80, Jan. 2020, doi: 10.1002/elps.201900286.
- [28] Z. Cheng and T. R. Savarimuthu, "A novel robot-assisted electrical impedance scanning system for subsurface object detection," *Meas. Sci. Technol.*, vol. 32, no. 8, Aug. 2021, Art. no. 085902, doi: 10.1088/1361-6501/abe480
- [29] L. Xu et al., "3D multifunctional integumentary membranes for spatiotemporal cardiac measurements and stimulation across the entire epicardium," *Nature Commun.*, vol. 5, no. 1, Feb. 2014, Art. no. ncomms4329.
- [30] V. Penza, Z. Cheng, M. Koskinopoulou, A. Acemoglu, D. G. Caldwell, and L. S. Mattos, "Vision-guided autonomous robotic electrical bio-impedance scanning system for abnormal tissue detection," *IEEE Trans. Med. Robot. Bionics*, vol. 3, no. 4, pp. 866–877, Nov. 2021, doi: 10.1109/TMRB.2021.3098938.
- [31] F. Zhao, X. Xu, and S. Q. Xie, "Computer-aided inspection planning—The state of the art," *Comput. Ind.*, vol. 60, no. 7, pp. 453–466, Sep. 2009, doi: 10.1016/j.compind.2009.02.002.
- [32] Y. Liu, W. Zhao, R. Sun, and X. Yue, "Optimal path planning for automated dimensional inspection of free-form surfaces," *J. Manuf. Syst.*, vol. 56, pp. 84–92, Jul. 2020, doi: 10.1016/j.jmsy.2020.05.008.
- [33] H. Zhao, J.-P. Kruth, N. Van Gestel, B. Boeckmans, and P. Bleys, "Automated dimensional inspection planning using the combination of laser scanner and tactile probe," *Measurement*, vol. 45, no. 5, pp. 1057–1066, Jun. 2012, doi: 10.1016/j.measurement.2012.01.037.
- [34] C. Mineo, S. G. Pierce, P. I. Nicholson, and I. Cooper, "Introducing a novel mesh following technique for approximation-free robotic tool path trajectories," *J. Comput. Des. Eng.*, vol. 4, no. 3, pp. 192–202, Jul. 2017, doi: 10.1016/j.jcde.2017.01.002.
- [35] Z. Zhao, Y. Li, and Y. Fu, "Collision-free path planning for efficient inspection of free-form surface by using a trigger probe," *Int. J. Adv. Manuf. Technol.*, vol. 120, nos. 3–4, pp. 2183–2200, May 2022, doi: 10.1007/s00170-022-08917-7.
- [36] A. Haleem and M. Javaid, "3D scanning applications in medical field: A literature-based review," Clin. Epidemiol. Global Health, vol. 7, no. 2, pp. 199–210, Jun. 2019.
- [37] A. Marro, T. Bandukwala, and W. Mak, "Three-dimensional printing and medical imaging: A review of the methods and applications," *Current Problems Diagnostic Radiol.*, vol. 45, no. 1, pp. 2–9, Jan. 2016.

- [38] B. N. Johnson and R. Mutharasan, "The origin of low-order and high-order impedance-coupled resonant modes in piezoelectric-excited millimeter-sized cantilever (PEMC) sensors: Experiments and finite element models," Sens. Actuators B, Chem., vol. 155, no. 2, pp. 868–877, Jul. 2011, doi: 10.1016/j.snb.2011.01.063.
- [39] H. Sharma, R. S. Lakshmanan, B. N. Johnson, and R. Mutharasan, "Piezoelectric cantilever sensors with asymmetric anchor exhibit picogram sensitivity in liquids," *Sens. Actuators B, Chem.*, vol. 153, no. 1, pp. 64–70, Mar. 2011, doi: 10.1016/j.snb.2010.10.006.
- [40] A. Canales et al., "Multifunctional fibers for simultaneous optical, electrical and chemical interrogation of neural circuits in vivo," *Nature Biotechnol.*, vol. 33, no. 3, pp. 277–284, Mar. 2015, doi: 10.1038/nbt.3093.
- [41] T. K. Bera, S. Bera, K. Kar, and S. Mondal, "Studying the variations of complex electrical bio-impedance of plant tissues during boiling," *Proc. Technol.*, vol. 23, pp. 248–255, Jan. 2016.
- [42] E. Kucukdeger et al., "Conformal 3D printing of non-planar antennas on wrinkled and folded Kapton films using point cloud data," *Flexible Printed Electron.*, vol. 6, no. 4, Dec. 2021, Art. no. 044002, doi: 10.1088/2058-8585/ac28f1.
- [43] Y. L. Kong et al., "3D printed quantum dot light-emitting diodes," *Nano Lett.*, vol. 14, no. 12, pp. 7017–7023, 2014.
- [44] B. N. Johnson et al., "3D printed anatomical nerve regeneration pathways," Adv. Funct. Mater., vol. 25, no. 39, pp. 6205–6217, Oct. 2015.
- [45] Y. Tong et al., "Low-cost sensor-integrated 3D-printed personalized prosthetic hands for children with amniotic band syndrome: A case study in sensing pressure distribution on an anatomical human-machine interface (AHMI) using 3D-printed conformal electrode arrays," PLoS ONE, vol. 14, no. 3, Mar. 2019, Art. no. e0214120.
- [46] M. Singh et al., "3D printed conformal microfluidics for isolation and profiling of biomarkers from whole organs," *Lab Chip*, vol. 17, no. 15, pp. 2561–2571, 2017.
- [47] Y. Huang et al., "Assembly and applications of 3D conformal electronics on curvilinear surfaces," *Mater. Horizons*, vol. 6, no. 4, pp. 642–683, 2019.
- [48] F. C. P. Sales, R. M. Ariati, V. T. Noronha, and J. E. Ribeiro, "Mechanical characterization of PDMS with different mixing ratios," *Proc. Struct. Integrity*, vol. 37, pp. 383–388, Jan. 2022, doi: 10.1016/j.prostr.2022.01.099.
- [49] M. Singh et al., "Closed-loop controlled photopolymerization of hydrogels," ACS Appl. Mater. Interface, vol. 13, no. 34, pp. 40365–40378, Sep. 2021, doi: 10.1021/acsami.1c11779.
- [50] A. P. Haring et al., "Real-time characterization of hydrogel viscoelastic properties and sol-gel phase transitions using cantilever sensors," J. Rheol., vol. 64, no. 4, pp. 837–850, Jul. 2020, doi: 10.1122/8.0000009.
- [51] E. Cesewski, M. Singh, Y. Liu, J. Zhang, A. P. Haring, and B. N. Johnson, "Real-time monitoring of hydrogel rheological property changes and gelation processes using high-order modes of cantilever sensors," *J. Appl. Phys.*, vol. 128, no. 17, Nov. 2020, Art. no. 174502, doi: 10.1063/5.0020547.
- [52] A. L. Chin et al., "Implantable optical fibers for immunotherapeutics delivery and tumor impedance measurement," *Nature Commun.*, vol. 12, no. 1, p. 5138, Aug. 2021, doi: 10.1038/s41467-021-25391-z.
- [53] C. Chaibundit, N. M. P. S. Ricardo, F. D. M. L. L. Costa, S. G. Yeates, and C. Booth, "Micellization and gelation of mixed copolymers P123 and F127 in aqueous solution," *Langmuir*, vol. 23, no. 18, pp. 9229–9236, Aug. 2007, doi: 10.1021/la701157j.

- [54] B. Van Lancker, W. De Corte, and J. Belis, "Material properties of a structural silicone for linear adhesive glass-metal connections," in *Proc. Challenging Glass Conf.*, vol. 5, 2016, pp. 363–372.
- [55] A. D. Lee, P. Shepherd, M. C. Evernden, and D. Metcalfe, "Measuring the effective Young's modulus of structural silicone sealant in moment-resisting glazing joints," *Construct. Building Mater.*, vol. 181, pp. 510–526, Aug. 2018, doi: 10.1016/j.conbuildmat.2018. 06.038.
- [56] J. Zhang et al., "Rapid, autonomous high-throughput characterization of hydrogel rheological properties via automated sensing and physicsguided machine learning," *Appl. Mater. Today*, vol. 30, Feb. 2023, Art. no. 101720, doi: 10.1016/j.apmt.2022.101720.
- [57] J.-L. Damez and S. Clerjon, "Quantifying and predicting meat and meat products quality attributes using electromagnetic waves: An overview," *Meat Sci.*, vol. 95, no. 4, pp. 879–896, Dec. 2013, doi: 10.1016/j.meatsci.2013.04.037.
- [58] S. C. Mukhopadhyay and C. P. Gooneratne, "A novel planartype biosensor for noninvasive meat inspection," *IEEE Sensors J.*, vol. 7, no. 9, pp. 1340–1346, Sep. 2007, doi: 10.1109/JSEN.2007. 903335
- [59] J. Lepetit and J. Culioli, "Mechanical properties of meat," *Meat Sci.*, vol. 36, no. 1, pp. 203–237, 1994, doi: 10.1016/0309-1740(94)90042-6.
- [60] N. Shoham, P. Girshovitz, R. Katzengold, N. T. Shaked, D. Benayahu, and A. Gefen, "Adipocyte stiffness increases with accumulation of lipid droplets," *Biophys. J.*, vol. 106, no. 6, pp. 1421–1431, Mar. 2014, doi: 10.1016/j.bpj.2014.01.045.
- [61] M. P. Chae, D. J. Hunter-Smith, S. V. Murphy, and M. W. Findlay, "3D bioprinting adipose tissue for breast reconstruction," in 3D Bioprinting for Reconstructive Surgery. Sawston, U.K.: Woodhead Publishing, 2018, pp. 305–353.
- [62] P. Zhuang, J. An, C. K. Chua, and L. P. Tan, "Bioprinting of 3D in vitro skeletal muscle models: A review," *Mater. Des.*, vol. 193, Aug. 2020, Art. no. 108794, doi: 10.1016/j.matdes.2020.108794.
- [63] B. Li, J. Lecourt, and G. Bishop, "Advances in non-destructive early assessment of fruit ripeness towards defining optimal time of harvest and yield prediction—A review," *Plants*, vol. 7, no. 1, p. 3, Jan. 2018, doi: 10.3390/plants7010003.
- [64] P. Sirisomboon, M. Tanaka, and T. Kojima, "Evaluation of tomato textural mechanical properties," *J. Food Eng.*, vol. 111, no. 4, pp. 618–624, Aug. 2012, doi: 10.1016/j.jfoodeng.2012.03.007.
- [65] N. Galili, I. Shmulevich, and N. Benichou, "Acoustic testing of avocado for fruit ripeness evaluation," *Trans. ASAE*, vol. 41, no. 2, pp. 399–407, 1998, doi: 10.13031/2013.17164.
- [66] K. K. Singh and B. S. Reddy, "Post-harvest physico-mechanical properties of orange peel and fruit," *J. Food Eng.*, vol. 73, no. 2, pp. 112–120, Mar. 2006, doi: 10.1016/j.jfoodeng.2005.01.010.
- [67] S. N. Jha, A. R. P. Kingsly, and S. Chopra, "Physical and mechanical properties of mango during growth and storage for determination of maturity," *J. Food Eng.*, vol. 72, no. 1, pp. 73–76, Jan. 2006, doi: 10.1016/j.jfoodeng.2004.11.020.
- [68] B. Bodakian and F. X. Hart, "The dielectric properties of meat," *IEEE Trans. Dielectr. Electr. Insul.*, vol. 1, no. 2, pp. 181–187, Apr. 1994, doi: 10.1109/94.300250.
- [69] E. Kucukdeger and B. N. Johnson, "Closed-loop controlled conformal 3D printing on moving objects via tool-localized object position sensing," J. Manuf. Process., vol. 89, no. 3, pp. 39–49, 2023.